



Lithium ion battery pack power fade fault identification based on Shannon entropy in electric vehicles

Yuejiu Zheng, Xuebing Han, Languang Lu, Jianqiu Li, Minggao Ouyang*

State Key Laboratory of Automotive Safety and Energy, Tsinghua University, Beijing 100084, PR China

HIGHLIGHTS

- The battery power fade fault in EV is discovered during the demonstration.
- The internal or contact resistance increase causes the EV power fade.
- Cell resistance fault is attributed to contact resistance using Shannon entropy.
- Proposed diagnostic method can be used without laboratory testing methods.

ARTICLE INFO

Article history:

Received 3 July 2012

Received in revised form

4 September 2012

Accepted 6 September 2012

Available online 13 September 2012

Keywords:

Electric vehicle
Lithium battery
Cell inconsistencies
Fault identification
Shannon entropy
Contact resistance

ABSTRACT

Fault diagnosis for inconsistent cells in a battery pack is important for electric vehicle (EV) safety. Discovering the fault and identifying its cause on-site are extremely challenging. The literature has rarely explored such issues. This paper presents a battery pack system in a demonstrated EV with 96 cells in series and discovers the battery power fade fault during the demonstration. The preliminary analysis, after collecting data and preprocessing the typical data periods, shows that the internal or contact resistance increase causes the fault. To further identify the fault cause, we introduce an equivalent circuit model (ECM) and identify the cell resistances using the total least squares algorithm. A diagnostic method is proposed, using the identified cell resistances from 3 months demonstration data. Calculating the Shannon entropy clearly identifies the cause of the power fade fault. Appropriate measures are taken to solve the fault, and the latent safety issue is eliminated. The proposed diagnostic method can be used on-site for EV diagnosis without laboratory testing methods.

© 2012 Elsevier B.V. All rights reserved.

1. Introduction

The merits of electric vehicles (EVs) have been recognized since people began to realize the energy crisis and environmental deterioration. The drawbacks of short driving ranges and high costs remain obstacles to the rise of EV industry. The disadvantages of EVs are inherited from the expensive power batteries and their energy densities [1]. Power batteries are thus generally considered the core technology in EVs. Moreover, a lack of methods and technologies in the battery safety issues conspicuously hinder the advance of battery application in EVs [2]. Safe technologies and fault diagnoses for power battery application in EVs gradually raise the attention.

* Corresponding author. Tel.: +86 10 62792797; fax: +86 10 62789699.

E-mail addresses: yuejiu.zheng@gmail.com (Y. Zheng), ouymg@tsinghua.edu.cn (M. Ouyang).

Research and literature on single-cell safety, including new electrode and electrolyte materials, remain the most discussed topics [3–6]. Other research focuses on the performance and safety of a single cell [7]. However, hundreds of single cells are connected in parallel and series to compose a battery pack and provide sufficient energy that can meet the power and energy required in an EV [8,9]. The similarity principle cannot be simply implemented from a single cell to the battery pack because of cell inconsistencies and mechanical integrity influences.

One crucial safety issue is thermal runaway. Initial cell ohmic internal resistance inconsistencies caused by manufacturing, contact resistance inconsistencies due to the module design or assembly issue [8] and inhomogeneous heat dissipation in the battery pack affect the thermal imbalance among cells. The thermal imbalance increases the inconsistent deterioration of the internal resistances [10]. Due to EV vibrations, the contact resistances vary if the connecting plate is not well bolted or welded [11]. The thermal runaway of the battery pack could thus occur without fault

diagnosis or prognosis. Consequently, to detect cell resistance inconsistencies in the battery pack, it is necessary to achieve fault diagnosis.

There are two methods for applying fault diagnosis technology: model- and data-based diagnosis [12]. This paper combines these methods to identify faults. An equivalent circuit model (ECM) is introduced and simplified, cell resistances are identified using data from a demonstrated EV and the fault cause is identified. Previous studies [13–23] have focused on one single cell or the whole battery pack, while few have examined dozens of cells under the assumption of inconsistent cells with data from a demonstrated EV for the purpose of fault diagnosis.

Yu-Hua Sun et al. [13,14] and Achmad Widodo et al. [15] proposed health auxiliary diagnosis methods for the lead-acid battery unit based on sample and approximate entropies. They concentrated on the discharge current and voltage without an ECM to predict the state of health (SOH). Jürgen Remmlinger et al. [16] developed an ECM and identified the internal resistance in a hybrid vehicle under the assumption of homogeneous cells and temperature. They concentrated on degradation using internal resistance by compensating for battery temperature influences. Oliver Bohlen et al. [17] also presented a method to predict the pulse power capability of a battery using an impedance-based battery model. The resistance or the impedance derived from ECM in previous studies [16,17] did not involve the contact resistance between the cells. Peyman Taheri et al. [11] investigated the energy loss due to the contact resistance in Li-ion battery assemblies for the first time.

The above studies did not focus on cell inconsistencies. Studies on cell inconsistencies in battery packs and their safety have been performed since 2011. Michael A. Roscher et al. [24] considered cells in battery pack individually and derived on-board methods to allow determining the impedance and state of charge (SOC) for many particular cells in a battery system. Gi-Heon Kim et al. [2] analyzed an internal short circuit response model for multi-cell packs and introduced a methodology for electrically isolating a faulty cell from the healthy cells.

Gregory J. Offer et al. [8] focused on diagnosing problems related to cells connected in parallel for motorsports application. They demonstrated a full vehicle test and found that one individual cell resistance increased due to the internal or contact resistance increase. They used electrochemical impedance spectroscopy (EIS) to test the suspected cells in the laboratory and verified that the contact resistance caused the uneven current flow within the pack. They also simulated this phenomenon using a battery module model, considering contact resistances.

This paper highlights fault diagnosis for the inconsistent cells in the battery pack. Individual cell resistances are defined as the sum of the internal and contact resistances. The cell resistances are identified using a simplified ECM. A diagnostic method is developed to distinguish between the internal and contact resistance increase faults, using historical data of the estimated individual cell resistances without laboratory testing methods.

2. Date collection and fault discovery

2.1. Data collection and preprocessing

An electric SUV made by a Chinese company was modified. A new pack with a new battery management system (BMS) replaced the original battery pack at the bottom of the EV. The new battery pack contains 96 single commercial LiFePO₄ cells in series (see Appendix A for more information). A modular BMS provided by Keypower Ltd. was applied to monitor and protect the battery pack (see Appendix B for more information). Data from 3 months, from

May 8 to July 29, 2011, were evaluated to analyze the performance of the battery pack and individual cells. The EV operates in 3 states: driving, charging and idle. As the demonstrated EV does not have a regenerative braking system, the battery pack always discharges during driving. The EV's driving state can thus be called a dynamic discharge period due to its battery pack behavior. The charging and idle states of the EV correspond to constant current charge and stand-by periods, respectively, due to battery pack behaviors.

There are 11 typical constant current charge periods that the battery pack started charging at low SOCs (<30%) and ended at a fully charged state from May 8 to July 29, 2011. Fig. 1(a) shows one of the 11 typical constant current charge periods. The charge process was controlled at a constant charge current of approximately 6 A. The charge process stopped when one cell reached the charge cutoff voltage, i.e., 3.6 V for a LiFePO₄ battery, as recommended by the battery manufacturer. Overcharge happened if the cell voltage exceeds 3.6 V, which would raise severe safety problems.

15 Typical dynamic discharge periods were found during the evaluation time. Fig. 1(b) shows one of the 15 typical dynamic discharge periods, found on May 9 at 15:28. The current changed acutely during the driving period because the EV accelerated frequently. Consequently, all 96 cell voltages dropped when the

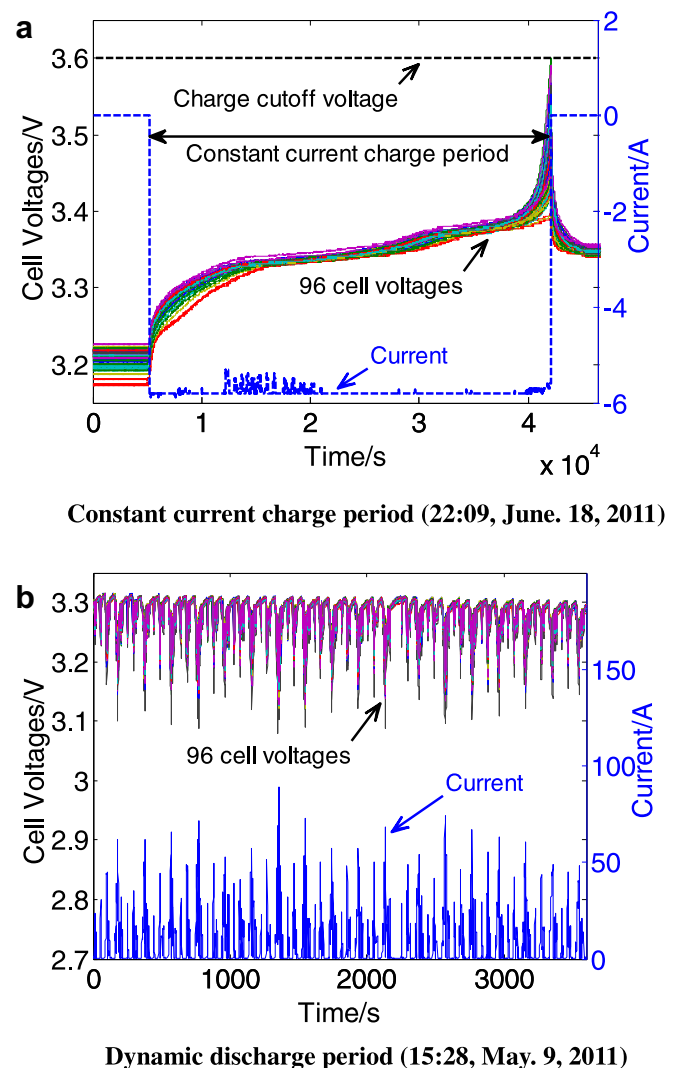


Fig. 1. Typical charging and discharging period during demonstration.

current rose. The cell voltages did not reach the discharge cutoff voltage of 2.5 V. Otherwise, over-discharge occurred, which can undoubtedly decrease the battery life time or even result in safety issues. The vehicle control algorithm should be responsible for this voltage limit by constraining the current to prevent the cell voltages from dropping significantly; the output power is limited if the cell voltages drop near to the discharge cutoff voltage.

2.2. Fault discovery and preliminary analysis

The EV power performance dropped to some extent in June according to the driving experience. This did not draw enough attention until analyzing data from the battery pack from May to July.

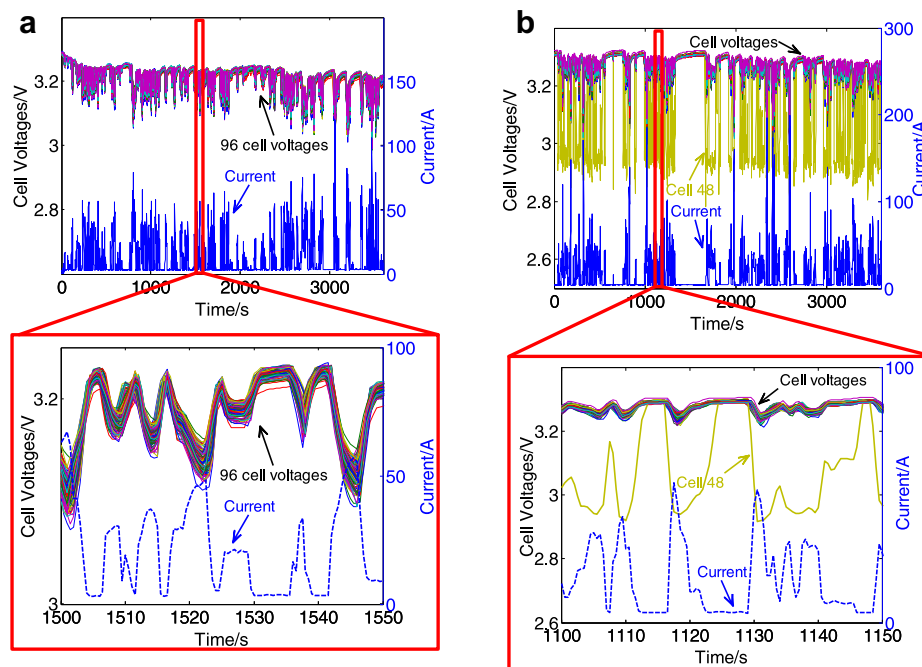
Fig. 2(a) shows one of the dynamic discharge periods before the fault. The time window is from 09:21 (time axis is labeled as 0) to 10:21, May 26, 2011. An inspection of the 50-s window starting at 1500 s is shown in the red rectangle. The first current peak of 67 A pulled all cell voltages down to approximately 3.1 V, for a voltage difference of approximately 50 mV. In contrast, Fig. 2(b) depicts one of the dynamic discharge periods after the fault. The time window is from 09:50 (time axis is labeled as 0) to 10:50, June 8, 2011. An inspection of the 50-s window starting at 1100 s is shown in the red rectangle. The voltage of cell 48 dropped significantly with the rising current. It dropped from 3.29 V to 2.94 V at a current of 55 A at 1118 s. Voltages of the other cells remained as high as approximately 3.24 V. Because the voltage of cell 48 was under 3 V, the vehicle control unit (VCU) automatically constrained the maximum power output to protect the battery pack from latent over-discharge. The power fade fault occurred as a result.

If resistances and voltage sources are used to represent the cell as an illustration, the equation $R = \Delta U / \Delta I$ is implemented to calculate the cell resistance. The comparison of the cell voltages in Fig. 2 shows a large cell resistance increase for cell 48. The voltage fault for cell 48 may be either caused by cell voltage measurement fault or the cell resistance increase.

Fig. 3(a) depicts the cell connections and voltage measurement, showing the schematic diagram of 3 cells in the battery pack. The cells are connected in series, and the connecting plates and measuring wire are bolted onto the cells' electrodes. Fig. 3(b) further describes the simple ECM of the cell connections and voltage measurement. $R_{i,N}$ represents the ohmic internal resistance for cell N. E_N is the open circuit voltage (OCV) for cell N. $R_{c,N+}$ and $R_{c,N-}$ are the contact resistances at the cathode and anode electrodes, respectively. The impedance of the measuring wire is replaced by the resistance $R_{m,N}$. The power current I flows through cells and connecting plates, but the current through the measuring wire i is extremely small as the impedance of the voltage measuring sensor is large. As a result, the IR drop through the measuring wire can be neglected and the measured voltage U_N is accurate enough as the cell voltage. As the measuring current i is independent of the power current I , the voltage of cell 48 is independent of the power current I if a cell voltage measurement fault happens. Assuming a measuring fault occurs between cells N and N + 1, there should be two voltage measurement faults (U_N and U_{N+1}) in such a configuration. This would conflict with the sole existence of the voltage fault in cell 48.

After the preliminary analysis, we conclude that the cell voltage measurement does not cause the power fade fault and hypothesize that the voltage fault in cell 48 may be caused either by the abnormal internal or contact resistance increase. Vehicle applications require distinguishing between the internal and contact resistance increase faults, as the corresponding measures differ. However, this task is difficult due to the similar behaviors in cell voltages of the internal and contact resistance increase faults, and their orders of magnitude are comparable. The normal internal resistance is less than 1 m Ω , and the contact resistance is measured in $\mu\Omega$ if correctly connected [8]. However, faulty contacts or abnormal internal resistance leads to much higher resistance, in the order of m Ω .

For the vehicle diagnosis application, on-site diagnosis would be acceptable if on-board diagnosis cannot be applied. However, the



Dynamic discharge period before the fault (09:21, May, 26, 2011) Dynamic discharge period after the fault (09:50, June, 8, 2011)

Fig. 2. Comparison of the discharge cell voltages before and after the fault.

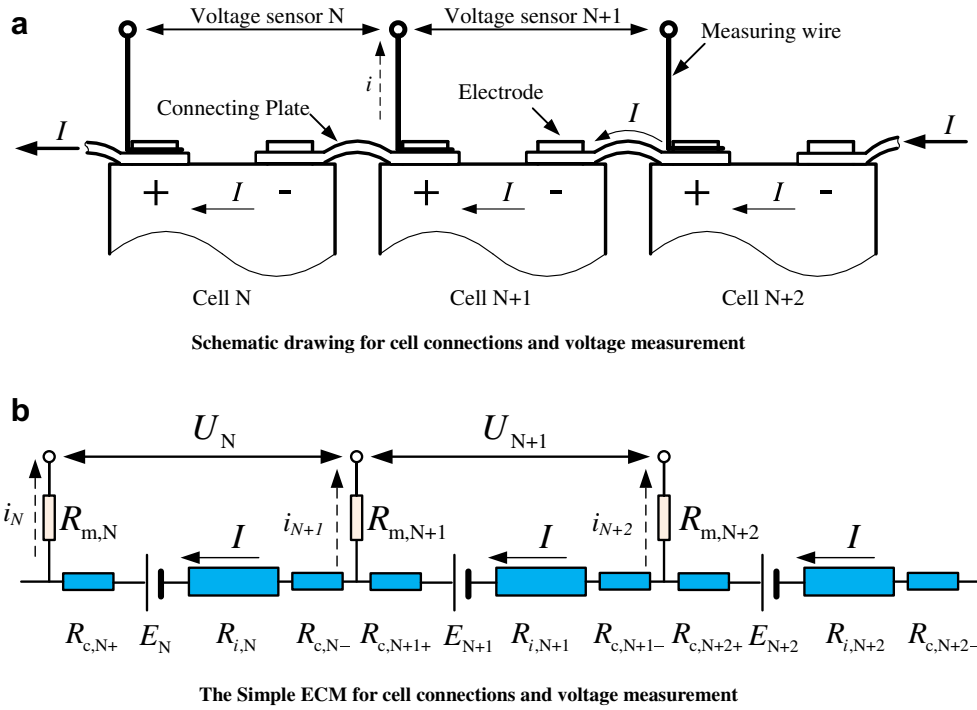


Fig. 3. Schematic diagram and simple ECM for cell connections and voltage measurement.

two similar faults are usually identified using laboratory tests [8]. No on-site diagnosis has yet been proposed to identify faults caused by the abnormal internal resistance increase or the contact resistance increase. This paper develops an on-site diagnosis using a battery model based on the characteristics of the contact resistance in the vehicle.

3. Battery modeling

3.1. Battery ECM considering contact resistance

The electrical behavior of a battery pack can be generally described using an equivalent circuit model (ECM). If cell inconsistencies are considered, describing every individual cell with its unique ECM and parameters is desirable. However, it takes time to experiment on every individual cell to fit a precise ECM. ECM precision is also questionable. Moreover, with different ECMs implemented on individual cells, the identified parameters among cells are not comparable. As a compromise, this paper uses one ECM for every single cell, and the differences between the identified parameters are used to reflect cell inconsistencies.

Fig. 4(a) proposes an ECM considering self-discharge rate. The 4 parts in the circuit are an ideal voltage source E , ohmic resistance R_i , parallel connection of an ohmic resistor R_p with a capacitor C_p , usually called RC-parallel connection, and ohmic resistance R_l connected in parallel.

The ideal voltage source E represents OCV, which depends on SOC and temperature or, more exactly, the percentage of active materials in both electrodes. In a short time interval, the ideal voltage source E can be considered a constant value, as SOC and temperature do not change much. The ohmic resistance R_i stands for the cell internal resistance, which is temperature- and degradation-dependent. The RC-parallel connection represents the effects caused by polarization. The RC-parallel connection parameters depend on temperature and degradation as well as SOC. Finally, an ohmic resistance R_l connected in parallel represents the self-discharge rate, which is primarily influenced by temperature and OCV [25].

The state equation of this ECM is thus:

$$\begin{aligned} \dot{U}_{C_p} &= -\frac{1}{C_p} \left(\frac{1}{R_l + R_i} + \frac{1}{R_p} \right) \cdot U_{C_p} + \frac{R_l}{(R_l + R_i)C_p} \cdot I + \frac{1}{(R_l + R_i)C_p} \cdot E \\ U &= -\frac{R_l}{R_l + R_i} \cdot U_{C_p} - \frac{R_l R_i}{R_l + R_i} \cdot I + \frac{R_l}{R_l + R_i} \cdot E \end{aligned} \quad (1)$$

Although the state equation is clearly stated, the self-discharge resistance R_l cannot be easily identified. Self-discharge is a long-term effect with a time constant counted in days, while time constants for the other parameters are measured in seconds. Realistic calculations thus usually neglect the self-discharge resistance R_l .

Moreover, it is necessary to add an electric contact resistance to the existing ECM to present the contact resistances in the battery pack connections, as the contact resistances are comparable to internal resistances and cannot be neglected. Fig. 4(b) shows an evolved ECM considering the contact resistances R_{c+} and R_{c-} and ignoring the self-discharge resistance R_l .

Fig. 4(c) introduces a simplified widely used Thevenin ECM. The cell resistance R'_i gives the contact resistances R_{c+} and R_{c-} along with the cell internal resistance R_i , i.e., $R'_i = R_i + R_c$.

The state equation of Thevenin ECM is given as follows.

$$\begin{aligned} \dot{U}_{C_p} &= -\frac{1}{C_p R_p} \cdot U_{C_p} + \frac{I}{C_p} \\ U &= -U_{C_p} - I R'_i + E \end{aligned} \quad (2)$$

The state equation is expressed in the linear discrete system as the discrete state space equation:

$$\begin{aligned} U_{C_p}((k+1)T) &= e^{-\frac{T}{C_p R_p}} \cdot U_{C_p}(kT) + \left(1 - e^{-\frac{T}{C_p R_p}}\right) R_p \cdot I(kT) \\ U(kT) &= -U_{C_p}(kT) - R'_i \cdot I(kT) + E, \end{aligned} \quad (3)$$

where T is the sampling time and kT is the time series. With this discrete state space equation, parameters can be estimated using optimal state estimation.

3.2. Model parameter identification

The difference equation (4) is deduced from the discrete state space equation (3) by eliminating U_{cp} .

$$U((k+1)T) = e^{-\frac{T}{C_p R_p}} \cdot U(kT) + \left[e^{-\frac{T}{C_p R_p}} \cdot R'_i - \left(1 - e^{-\frac{T}{C_p R_p}}\right) R_p \right] \cdot I(kT) - R'_i \cdot I((k+1)T) + \left(1 - e^{-\frac{T}{C_p R_p}}\right) E \quad (4)$$

The difference equation (4) can be written as equation (5)

$$U((k+1)T) = x_1 \cdot U(kT) + x_2 \cdot I(kT) + x_3 \cdot I((k+1)T) + x_4, \quad (5)$$

where

$$\begin{cases} x_1 = e^{-\frac{T}{C_p R_p}} \\ x_2 = e^{-\frac{T}{C_p R_p}} \cdot R'_i - \left(1 - e^{-\frac{T}{C_p R_p}}\right) R_p \\ x_3 = -R'_i \\ x_4 = \left(1 - e^{-\frac{T}{C_p R_p}}\right) E \end{cases} \quad (6)$$

From equation (6), the parameters are

$$\begin{cases} R'_i = -x_3 \\ E = \frac{x_4}{1 - x_1} \\ R_p = \frac{-x_2 - x_1 x_3}{1 - x_1} \\ C_p = \frac{T}{\frac{-x_2 - x_1 x_3}{1 - x_1} \cdot \log x_1} \end{cases} \quad (7)$$

To identify the parameters, the equation (5) can be written as

$$\mathbf{u} = A\mathbf{x}, \quad (8)$$

$$\text{where } \mathbf{x} = \begin{bmatrix} x_1 \\ x_2 \\ x_3 \\ x_4 \end{bmatrix}, \mathbf{u} = \begin{bmatrix} U((k+1)T) \\ \dots \\ U((k+n)T) \end{bmatrix} \text{ and } A = \begin{bmatrix} U(kT) & I(kT) & I((k+1)T) & 1 \\ \dots & \dots & \dots & \dots \\ U((k+n-1)T) & I((k+n-1)T) & I((k+n)T) & 1 \end{bmatrix}.$$

\mathbf{u} is a set of n sampling time series of $U((k+1)T)$. Sampling time T is 0.5 s, according to the data recorded. n is carefully determined. A large n is beneficial for the estimation accuracy; the hypothesis that the estimated parameters are constant is suspicious, as a large n makes the time interval too long to neglect parameter changes.

\mathbf{x} is estimated using optimal state estimation. The least squares algorithm is the simplest method using a generalized inverse matrix, but the solution is biased because matrix A is considered to have no stochastic error. The total least squares algorithm is implemented, which considers the error of matrix A . The solution of the total least squares algorithm is believed to be theoretically unbiased [26]. We reformulate equation (8) with the measurement error thus:

$$\mathbf{u} + E_u = (A + E_A)\mathbf{x}, \quad (9)$$

where E_u and E_A are the measurement error matrices of \mathbf{u} and A , respectively. The problem lies in finding an \mathbf{x} that minimizes error

matrices E_u and E_A for \mathbf{u} and A , respectively. We can solve the problem by minimizing $\| [E_A \ E_u] \|_F$, where the operator $\| \bullet \|_F$ is the Frobenius norm. The singular value decomposition (SVD) is used for this purpose, i.e., $[A \ \mathbf{u}] = U\Sigma V^T$, where $\Sigma = \text{diag}(\sigma_1, \sigma_2, \dots, \sigma_n, \sigma_{n+1})$ and $\sigma_1 \geq \sigma_2 \geq \dots \geq \sigma_n \geq \sigma_{n+1} \geq 0$. The solution of the total least squares algorithm is deduced from the last column of matrix V [26]:

$$\hat{\mathbf{x}} = \frac{1}{v_{n+1, n+1}} [v_{1, n+1}, \dots, v_{n, n+1}]^T \quad (10)$$

3.3. Parameter evaluation

Dynamic discharge period data collected over 3 months, from May to July 2011, are used to identify the model parameters. Parameters from 15 typical dynamic discharge periods are examined. The earliest of the 15 dynamic discharge periods and the dynamic discharge period after the power fade fault are depicted to discover preliminary results. We concentrate more on cell resistances because the cell resistance is temperature- and degradation-dependent and there is little correlation between SOC and cell resistance. Historical data about cell resistance are comparable if the temperature compensation is appropriately made. The cell resistance fault diagnosis is expected by comparing historical cell resistances.

Fig. 1(b) shows the cell voltages and current for the earliest of the 15 dynamic discharge periods (15:28, May 9, 2011). The cell resistances plotted in Fig. 5(a) are achieved when cell voltages and current shown in Fig. 1(b) are substituted into formulas (7), (8) and (10). The curves of the identified cell resistances are relatively flat, as the temperature remains approximately unchanged during the time interval. The cell resistance for cell 49 is larger than others in this dynamic discharge period. We investigate the temperature difference and find that cell 49 is not at a much lower temperature, at which point the cell resistance increases slightly. However,

a larger cell resistance for cell 49 is still possible due to the contact condition in the vehicle or manufacturing process.

As the cell resistance stays approximately constant relative to time, we use cell resistance averaged over an hour duration to further investigate the cell resistances. Fig. 5(b) presents the distribution of an hour average cell resistances. The mean cell resistance value is 0.5593 mΩ, and the standard deviation is 0.0861 mΩ. Almost all cell resistance values are in the range of 3-Sigma, except cell 49.

As the EIS test was performed for the cell screening procedure at room temperature, we can use the EIS test results to evaluate the precision for the identified cell resistances. Fig. 6(a) shows the EIS for 96 cells. The intersections of the EIS curves with the real axis are assumed to be cell resistances [27]. Fig. 6(b) investigates the test cell resistance distribution. All test cell resistances are screened in the 3-Sigma range and lower than 1 mΩ. The mean value of 96 test cell resistances is 0.5255 mΩ, and the standard deviation is 0.1023 mΩ.

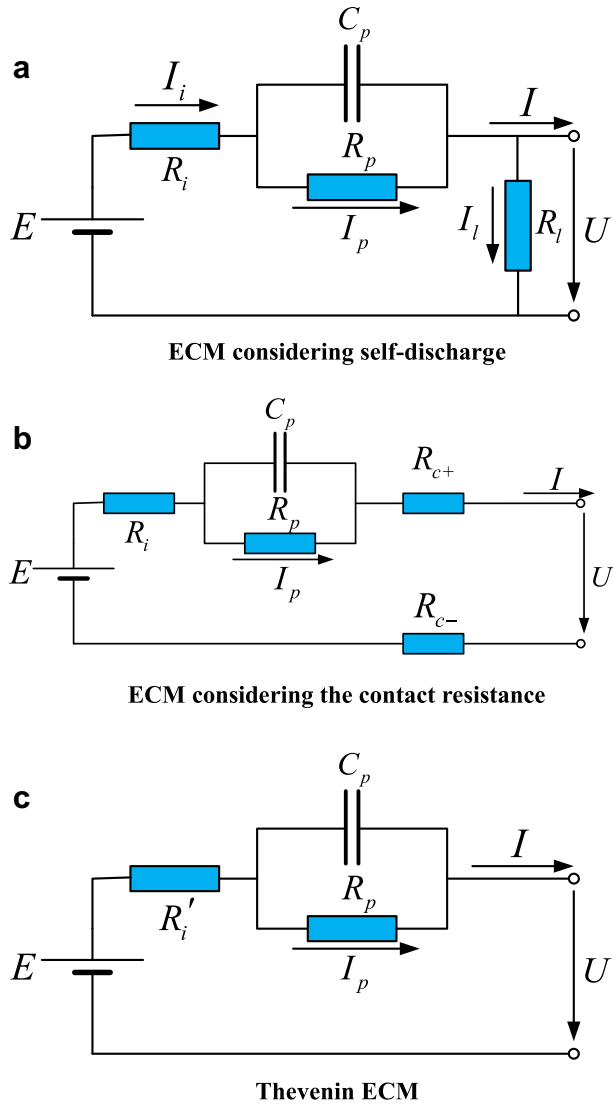


Fig. 4. Battery ECM considering contact resistance.

Compared to the test cell resistances, the identified cell resistances are slightly larger for two reasons. First, the test cell resistances are tested at room temperature, i.e., 25 °C, and the identified cell resistances are achieved at temperatures below room temperature, which could make the identified cell resistances larger. The other reason is that the cells in the EIS test have much better contact conditions than those in the battery pack with vibrations. Nevertheless, the differences between the identified and test cell resistances are still under 0.1 mΩ, which proves that the identified cell resistances are reliable for vehicle application.

The cell resistances of the other 14 dynamic discharge periods are also identified using the same method as those of the earliest of the 15 dynamic discharge periods. Fig. 7 shows the cell resistances from the dynamic discharge period after the power fade fault to discover the cell resistance behavior of the power fade fault. All other cell resistances stay constant, and the values are in the range of 0.3 mΩ–0.8 mΩ, except cell 48. The resistance of cell 48 differs from that of other cells: it is much larger than 1 mΩ and changes acutely relative to time. The identified resistance of cell 48 in Fig. 7 supports the analysis in Section 2.2: the cell resistance increase causes the power fade fault.

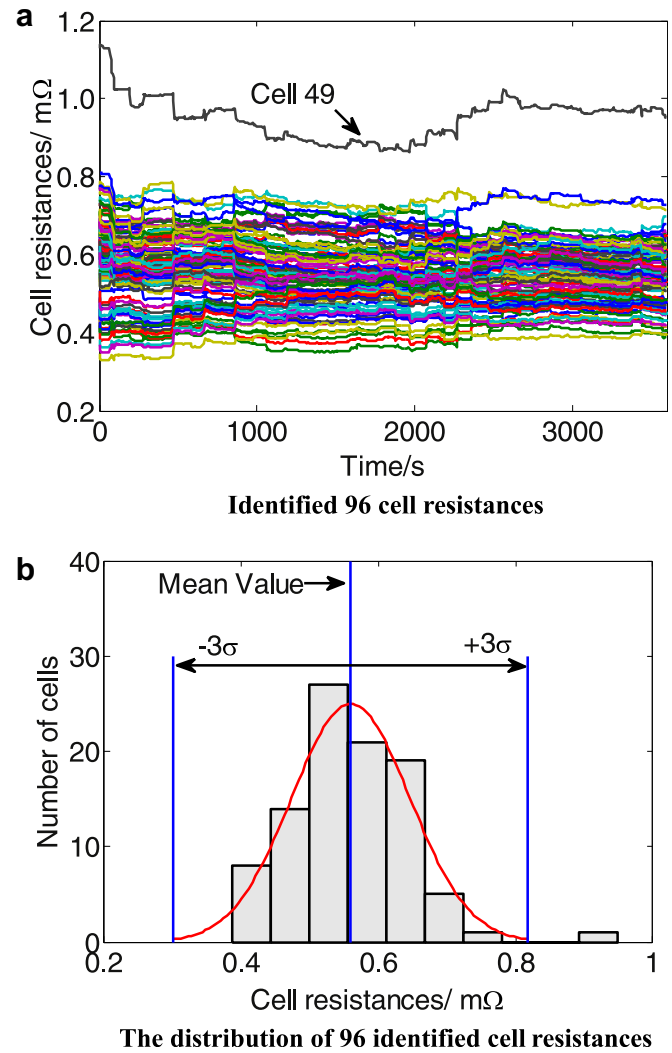


Fig. 5. Identified 96 cell resistances and their distribution (15:28 May 9, 2011).

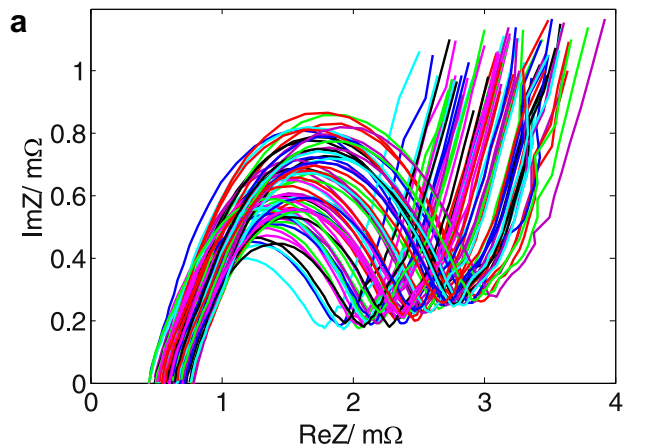
4. Fault identification and solution

4.1. Cell resistance fault identification

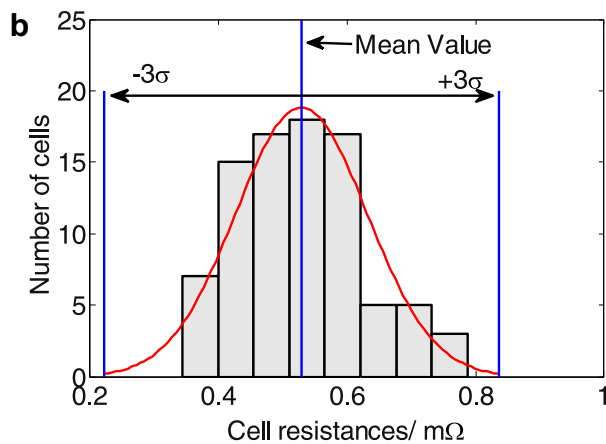
As stated in Section 2.2, cell resistance fault identification is challenging due to the similar behaviors of the internal and contact resistance increase faults. The cell resistance fault is usually identified in the laboratory. With historical data about the estimated cell resistances, we try to develop a method to distinguish between the internal and contact resistance faults.

Though electrical behaviors of the internal and contact resistance increase faults are similar, the differences do exist. The increasing internal resistance is caused by degrading cell electrochemistry and is thus slow time-varying. Growth of the SEI (solid electrolyte interface) film, lattice deformation in electrodes and electrochemical deposition in electrolytes gradually increase the internal resistance, and this increase is irreversible. Contact pressure significantly affects contact resistance, and poor contact conditions increase the contact resistance. Especially in vehicle applications, contact pressure variation due to vehicle vibration makes the contact resistance highly unstable if poor contact conditions occur.

To identify the cell resistance fault, we must investigate cell resistance behavior within a span of time to distinguish between



EIS of the screened 96 cells before demonstration (25°C)



The distribution of EIS test cell resistances

Fig. 6. EIS test of the screened 96 cells and their cell resistances distribution before demonstration (25 °C).

the internal and contact resistance faults. As temperature is the major factor affecting internal resistance, the temperature influence should be compensated for or eliminated. The laboratory measures the characteristics of the internal resistance of the LiFePO₄ cell used in the battery pack before demonstration using the HPPC (Hybrid Pulse Power Characterization) test. Fig. 8 shows

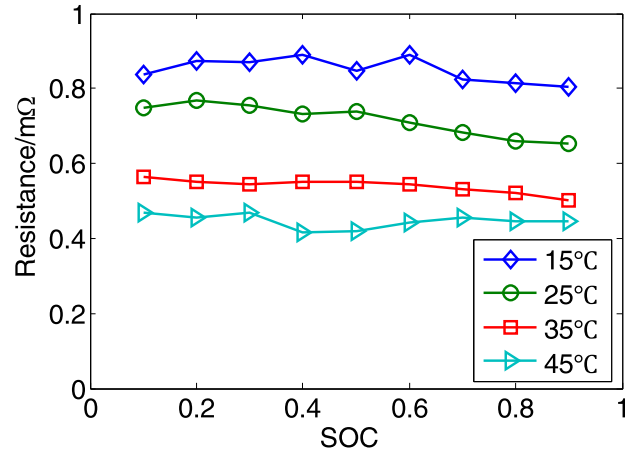


Fig. 8. The internal resistance characteristics of the LiFePO₄ cell used in the battery pack.

the results. The internal resistance is relatively flat with SOC and below 1 mΩ at room temperature, e.g., 25 °C. The internal resistance decreases when the temperature increases. Fig. 9 depicts the SOC mean internal resistance relative to temperature. In fact, the internal resistance follows an Arrhenius law with the temperature

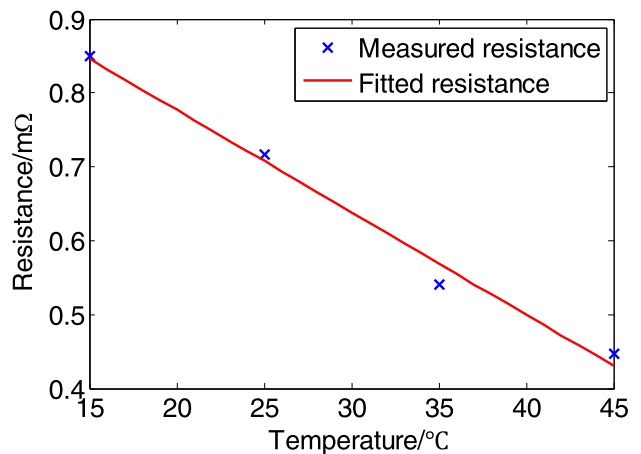


Fig. 9. Measured internal resistance relative to temperature.

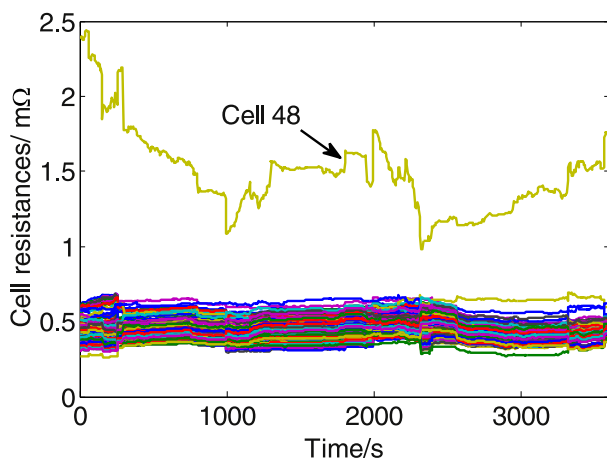


Fig. 7. Identified 96 cell resistances after the power fade fault (09:50, June, 8, 2011).

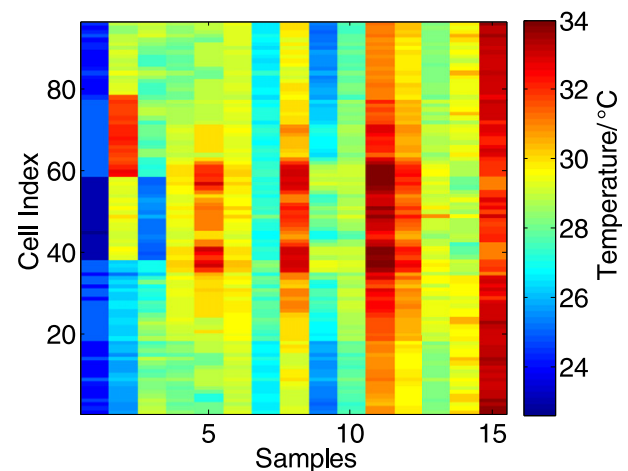


Fig. 10. Cell temperatures in the 15 dynamic discharge periods.

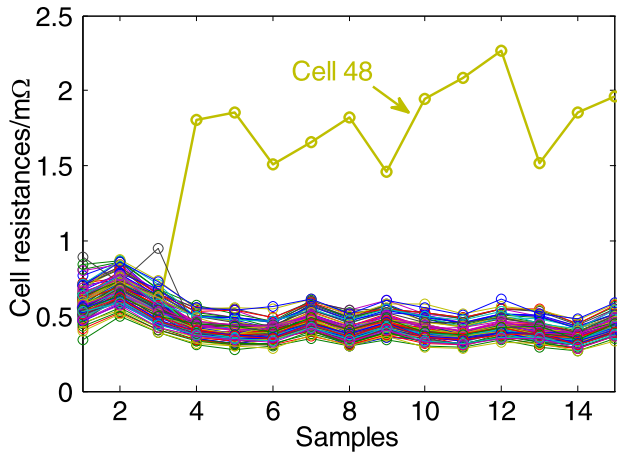


Fig. 11. Temperature compensated cell resistances during the 15 dynamic discharge periods.

change [16], and the low temperature internal resistance increases dramatically. However, as we use the battery pack in the temperature range of 15 °C–45 °C, the internal resistance changes approximately linearly. Linear fitting for temperature compensation is thus applied in this paper using equation (11):

$$R'_t = R'_{25} + k(t - 25), \quad (11)$$

where R'_t is the compensated cell resistance, R'_{25} is the cell resistance at 25 °C, t is the cell temperature and $k = -0.0138 \text{ m}\Omega \text{ } ^\circ\text{C}^{-1}$ is the compensation factor.

Temperatures and cell resistances of the individual cells during the 15 dynamic discharge periods are almost time-invariant because the time intervals are relatively short. The mean temperatures and cell resistances are used to represent the temperature and identified cell resistances in their respective dynamic discharge periods. Fig. 10 plots the mean temperature of each cell in the 15 dynamic discharge periods. The color map shows the temperature, with a maximum temperature of 34 °C and minimum of 22 °C. Each column shows the mean cell temperatures during one dynamic discharge period, so the temperatures in each column are close to each other. As the ambient temperature grows from May to July, the temperature along the horizontal axis grows overall. The temperature difference is not more than 12 °C, which is in the moderate working temperature range.

All cell resistances are compensated to the equivalent 25 °C cell resistances using equation (11). Fig. 11 shows the cell resistances with temperature compensation during the 15 dynamic discharge periods. All cell resistances are approximately constant except cell

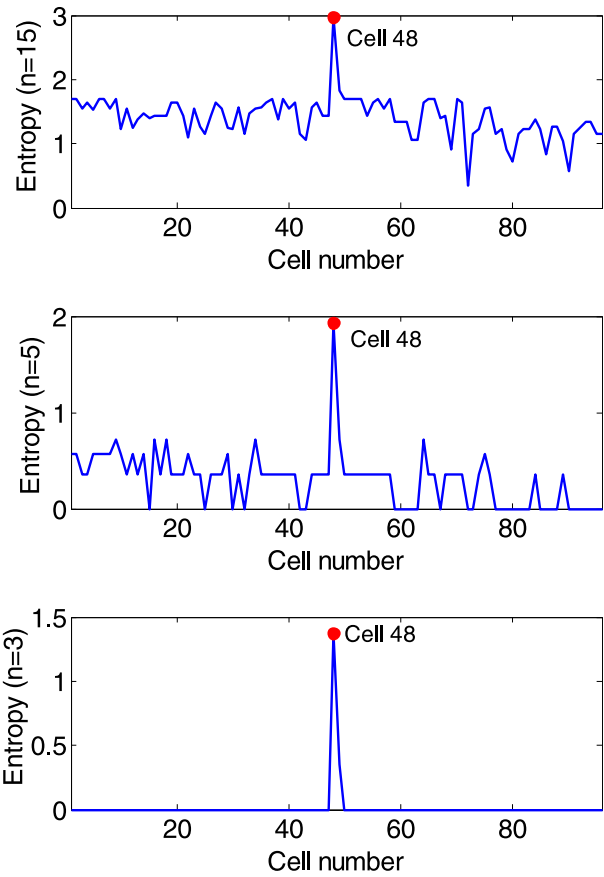


Fig. 13. Shannon entropies of 96 cell resistances in 15 dynamic discharge periods.

48, the cell resistance of which rises to a much higher level than the others from the fourth sample and varies fiercely during all samples. The earliest of the 15 dynamic discharge periods in Section 3.3 is the first sample in Fig. 11, and the dynamic discharge period after the power fade fault depicted in Section 3.3 is the fourth sample. A cell resistance fault occurs between the third and fourth samples. Fig. 12 shows the variability in the cell resistances of the 15 samples. The dataset for cell 48 is much looser than that for other cells.

The above two figures (Figs. 11 and 12) indicate a contact resistance fault in cell 48, as it varies during all samples and the dataset is much looser than that for other cells. This result completely matches the characteristics of the contact resistance fault, as the contact resistance is highly unstable due to the contact pressure variation in the vehicle application.

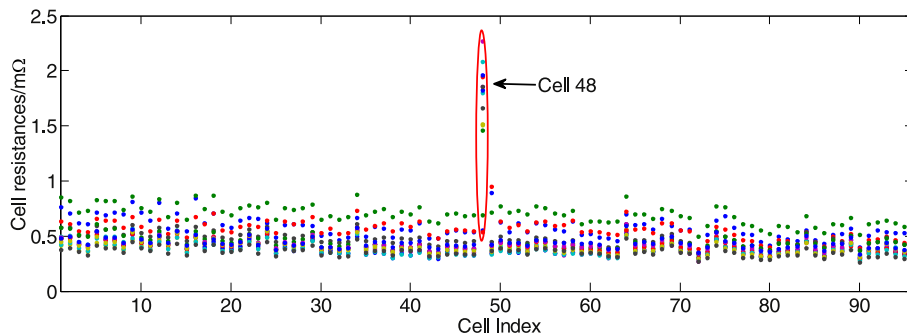


Fig. 12. Cell resistances inconstancies of the 96 cells.

A method using Shannon entropy and historical cell resistance data are developed to detect the contact resistance fault. A larger Shannon entropy value indicates the dataset distribution set is flatter, which means the dataset is looser. Conversely, a smaller Shannon entropy value means the data varies less. A larger Shannon entropy value for the cell resistance is thus more likely to be the contact resistance fault than the internal resistance fault. The formula of the Shannon entropy is

$$H(X) = - \sum_{i=1}^n p(x_i) \log p(x_i), \quad (12)$$

where $H(X)$ is the Shannon entropy, $p(x_i)$ is the probability density of data in the i th region and n is the number of the regions. The historical data about cell resistance entropy are calculated using different n values in equation (12), and Fig. 13 depicts the results.

From the calculation results, the entropies of cell 48 are always the largest, which means that the cell resistance of cell 48 varies more significantly than the others. When $n = 3$ in equation (12), the entropies of other cell resistances decrease to 0, but the entropy of cell 48 remains. From this perspective, the cell resistance increase fault is attributed to the contact resistance increase fault instead of the internal resistance increase fault.

4.2. Fault solution and results

After theoretically attributing the power fade fault to the contact resistance increase fault, the fault solutions were undertaken to

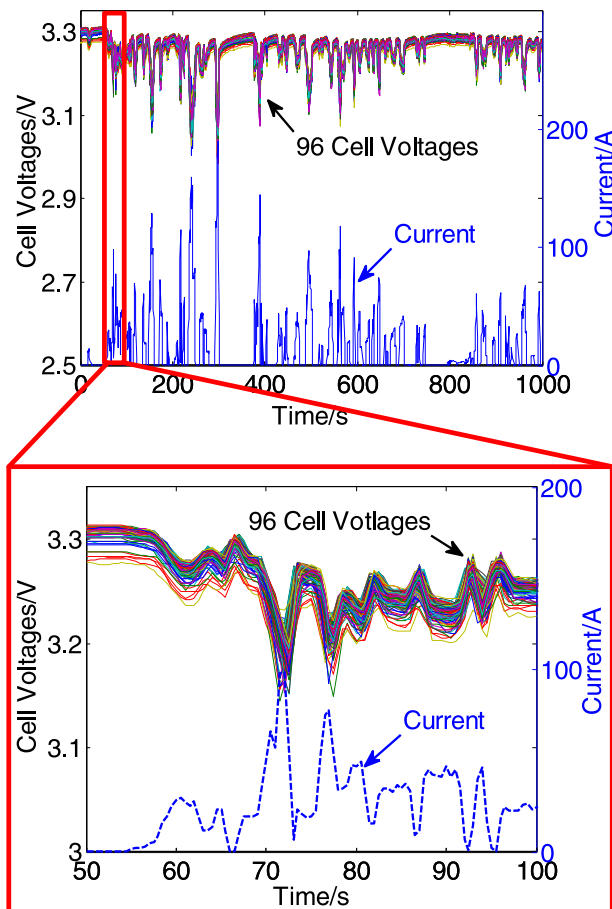


Fig. 14. Test run of dynamic discharge period after repair (11:16, Aug. 6, 2011).

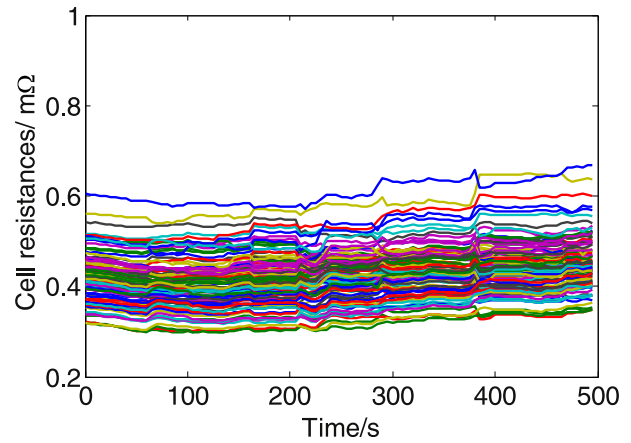


Fig. 15. Identified cell resistances after repair (11:16, Aug. 6, 2011).

solve the fault. The battery pack was unfolded, and two connecting plates of cell 48 were bolted again. After the repair, the vehicle underwent a 20 min test run, and the EV power performance returned to normal, according to the driving experience. Data from the test run were also recorded and analyzed using the same technology. Fig. 14 shows the test run for the dynamic discharge period after repair. An inspection of the 50-s window starting at 50 s is also shown in the red rectangle. The voltage of cell 48 has returned to normal, and the curve of cell 48 is submerged in the cluster of the 96-cell voltage curves. Cell resistances are investigated in Fig. 15, which also indicates the contact resistance increase fault has been repaired.

The contact resistance increase fault is attributed to faulty contacts. The contacts should be carefully designed in the vehicle application to avoid the contact resistance increase fault. Good battery pack integration is responsible to prevent this fault. Vibration reduction design and looseness-proof bolt are required to prevent the latent contact faults. The risk of the contact resistance increase will be greatly reduced if the contacts are welded. However, if the internal resistance increase happens, it would be complicated to replace a new cell. To prevent the internal resistance increase fault in vehicle application, the cells are strictly forbidden from abuse. BMS is responsible to prevent this fault. Over or under voltage is not allowed and BMS guarantees that cells are working at homogeneous temperature. These solutions will significantly reduce the risk of the internal and contact resistances increase. However, the internal or contact resistance increase cannot be eliminated and the diagnostic methods for the internal and contact resistance increase faults are still required.

5. Conclusion

This paper proposes a diagnostic method for EVs to distinguish between the internal and contact resistance increase faults by calculating the Shannon entropy of the estimated individual cell resistances without laboratory tests.

First, we present a battery pack system in a demonstrated EV with 96 cells in series and discover the battery power fade fault during the demonstration. After data collection and a preliminary analysis of the typical data periods, we conclude that the cell voltage measurement does not cause the power fade fault and hypothesize that the voltage fault may be either caused by the abnormal internal or contact resistance increases. The increasing internal resistance is caused by degrading cell electrochemistry and is thus slow time-varying and irreversible. However, the contact

resistance is significantly influenced by the contact pressure due to vehicle vibration.

To further identify the fault cause, individual cell resistances are defined as the sum of the internal and contact resistances. We introduce an equivalent circuit model and identify the cell resistances using the total least squares algorithm which is believed to be theoretically unbiased. The identified cell resistances are then compared to the EIS test and are proved to be reliable for vehicle application. A diagnostic method is developed to distinguish between the internal and contact resistance increase faults using the estimated individual cell resistances from 3 months of the demonstration data. By calculating the Shannon entropy, the cell resistance fault cause is attributed to the contact resistance fault. Finally, the corresponding measures are taken to solve the fault, thus verifying the proposed method.

Acknowledgments

This research is funded by the MOST (Ministry of Science and Technology) of China under the contract of No. 2010DFA72760, the Tsinghua University Initiative Scientific Research Program (Grand No. 2010THZ08116) and the Delta Science & Technology Educational Development Program. The authors appreciate the data provided by Keypower Technology Co, Ltd. as well.

Appendices

A. The demonstrated EV and its LiFePO₄ battery pack

An electric SUV made by a Chinese company was modified. A new pack with the new BMS replaced the original battery pack at the bottom of the EV. The refitted EV, shown in Fig. A.1(a), started its demonstration in April 2011 at the State Key Laboratory of Automotive Safety and Energy at Tsinghua University. This demonstration aimed to study the performance of the battery pack and its individual cells in real vehicle situations.

The new battery pack (Fig. A.1(b)) contains 96 single commercial LiFePO₄ cells in series. Table A.1 describes the LiFePO₄ cell characteristics and Table A.2 summarizes the pack specifications. The battery manufacturer guaranteed that all cell capacities were more than 70 Ah and the capacity differences were less than 5%. An EIS test was performed to screen the cell internal resistances as a screening procedure before grouping cells.

Table A.1

Characteristics of the LiFePO₄ cell.

Parameters (Units)	Values
Nominal capacity (Ah)	>70@0.3C discharge
Nominal voltage (V)	3.2
Internal resistance (mΩ)	<1
Maximum discharge current rate	5C(20 s), 1.5C(continuous)
Discharge cutoff voltage (V)	2.5
Rated charge current rate	1/3C
Maximum charge current rate	1C
Charge cutoff voltage (V)	3.6

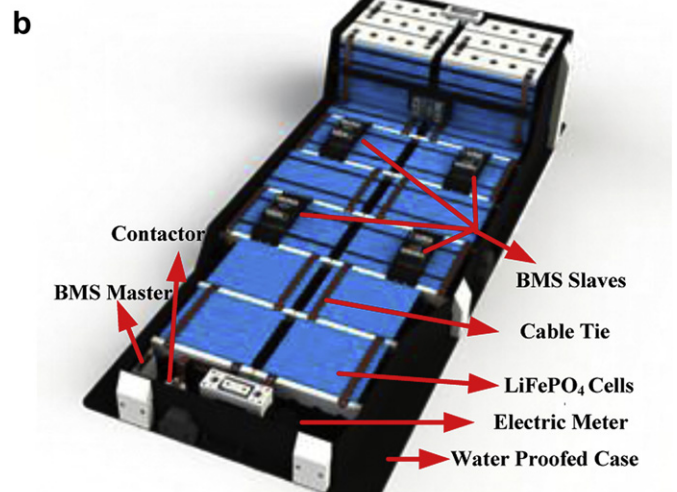
Table A.2

Battery pack specifications.

Parameters (Units)	Values
Nominal capacity (Ah)	70
Nominal voltage (V)	300
Watt hours (kW h)	21
Continuous discharge current (A)	105(1.5C)
Maximum power (kW)	31.5
Charge current (A)	6



The demonstrated EV under refit



The LiFePO₄ battery pack

Fig. A.1. The demonstrated EV and its battery pack.

B. The battery management system

As Fig. A.1(b) shows, a modular BMS provided by Keypower Ltd. was applied to monitor and protect the battery pack. The BMS mainly contains a master controller, 4 slave controllers, an electric meter and a data logger. Fig. B.1 depicts the BMS topology. The master controller is the communication center for two controller area network (CAN) buses. It is also the calculation center for the BMS. The BMS uses 4 slave controllers, and 24 channels in each slave controller are used to manage 24 cells. Each channel has one voltage sensor for individual cell voltage measurement and one temperature sensor for temperature measurement. In such a configuration, the voltages and temperatures of 96 cells were measured and sent through the BMS CAN bus. An electric meter is used to measure the current and pack voltage with a relatively high resolution. A CAN data logger was developed to record historical data from the BMS CAN bus every 0.5 s. Data are stored in the memory card and subsequently transferred to the computer for further processing.

Table B.1 shows the accuracy of all modular BMS signals. The accuracy is well qualified for vehicle application.

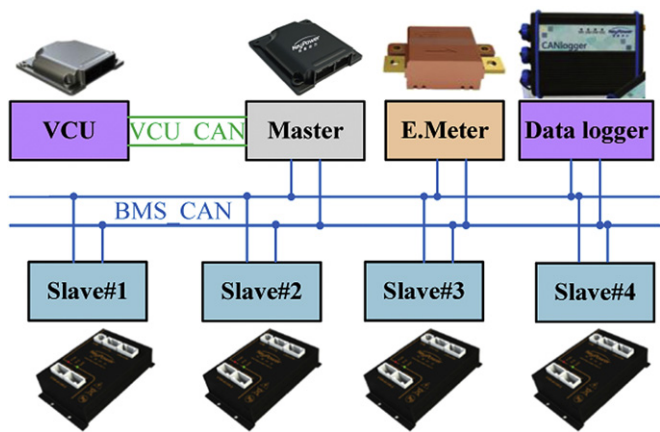


Fig. B.1. Topology of the BMS

Table B.1
Modular BMS signal accuracy.

Signals	Accuracy
Cell voltages	± 5 mV with a resolution 1 mV
Cell temperatures	± 1 °C
Current	0.1 A(<30 A) $\pm 1\%$ (>30 A)
Pack voltage	1%

References

[1] F.T. Wagner, B. Lakshmanan, M.F. Mathias, J. Phys. Chem. Lett. 1 (2010) 2204–2219.

[2] G.H. Kim, K. Smith, J. Ireland, A. Pesaran, J. Power Sources 210 (2012) 243–253.

[3] D. Aurbach, J. Power Sources 146 (2005) 71–78.

[4] Q. Wang, P. Ping, X. Zhao, G. Chu, J. Sun, C. Chen, J. Power Sources 208 (2012) 210–224.

[5] D.P. Abraham, E.P. Roth, R. Kostecki, K. McCarthy, S. MacLaren, D.H. Doughty, J. Power Sources 161 (2006) 648–657.

[6] D.P. Abraham, J. Liu, C.H. Chen, Y.E. Hyung, M. Stoll, N. Elsen, S. MacLaren, R. Twisten, R. Haasch, E. Sammann, I. Petrov, K. Amine, G. Henriksen, J. Power Sources 119–121 (2003) 511–516.

[7] J. Zhang, J. Lee, J. Power Sources 196 (2011) 6007–6014.

[8] G.J. Offer, V. Yufit, D.A. Howey, B. Wu, N.P. Brandon, J. Power Sources 206 (2012) 383–392.

[9] M.S. Wu, C.Y. Lin, Y.Y. Wang, C.C. Wan, C.R. Yang, Electrochim. Acta 52 (2006) 1349–1357.

[10] R. Mahamud, C. Park, J. Power Sources 196 (2011) 5685–5696.

[11] P. Taheri, S. Hsieh, M. Bahrami, J. Power Sources 196 (2011) 6525–6533.

[12] J.F. Hua, L.G. Lu, M.G. Ouyang, J.Q. Li, L.F. Xu, J. Power Sources 196 (2011) 5881–5888.

[13] Y.H. Sun, H.L. Jou, J.C. Wu, K.D. Wu, Appl. Energy 87 (2010) 3691–3698.

[14] Y.H. Sun, H.L. Jou, J.C. Wu, Energy Convers. Manag. 50 (2009) 2250–2256.

[15] A. Widodo, M.C. Shim, W. Caesarendra, B.S. Yang, Expert Syst. Appl. 38 (2011) 11763–11769.

[16] J. Remmlinger, M. Buchholz, M. Meiler, P. Bernreuter, K. Dietmayer, J. Power Sources 196 (2011) 5357–5363.

[17] O. Bohlen, S. Buller, R.W. De Doncker, 2004 35th AMW IEEE Power Electronics Specialists Conference. Aachen, Germany, 2004, 2792–2797.

[18] F. Huet, J. Power Sources 70 (1998) 59–69.

[19] X.D. Zhang, R. Grube, K.K. Shin, M. Salman, R.S. Conell, Control Eng. Pract. 19 (2011) 555–563.

[20] Y.H. Chiang, W.Y. Sean, J.C. Ke, J. Power Sources 196 (2011) 3921–3932.

[21] H. He, R. Xiong, H. Guo, Appl. Energy 89 (2012) 413–420.

[22] M. Dürr, A. Cruden, S. Gair, J.R. McDonald, J. Power Sources 161 (2006) 1400–1411.

[23] W. He, N. Williard, M. Osterman, M. Pecht, J. Power Sources 196 (2011) 10314–10321.

[24] M.A. Roscher, O.S. Bohlen, D.U. Sauer, IEEE Trans. Energy Convers. 26 (3) (2011) 737–743.

[25] T. Utsunomiya, O. Hatozakib, N. Yoshimotoa, M. Egashiraa, M. Morita, J. Power Sources 196 (2011) 8598–8603.

[26] G.H. Golub, C.F. Van Loan, SIAM J. Numer. Anal. 17 (6) (1980) 883–893.

[27] J.R. Miller, Electrochim. Acta 52 (2006) 1703–1708.